EFFECT OF WELDING SETTINGS ON MECHANICAL CHARACTERISTICS, MICROSTRUCTURAL FEATURES, AND CORROSION PERFORMANCE IN FRICTION STIR WELDING OF DISSIMILAR AA6082-T6/7075-T6 JOINTS

Rasha M. Afify*, Mohammed Gamil

Department of Mechanical Engineering, Faculty of Engineering at Shoubra, Benha University, Cairo 11629, Egypt

*Correspondence: rasha.ali@feng.bu.edu.eg

ABSTRACT

This research explores the influence of welding settings (tool rotational speed, travel speed) on mechanical characteristics (tensile, micro-hardness), microstructure, and corrosion performance of dissimilar butt joints between aluminum alloys AA7075-T6 and AA6082-T6, which were fabricated by friction stir welding (FSW). The study considers three varied tool rotational speeds (1600, 2000, and 2300 rpm) in conjunction with three varied tool travel speeds (30, 40, and 50 mm/min). The butt joints were created by welding plates that were 6 mm thick. The welded specimens underwent characterization through optical microscopy, SEM, tensile testing, micro-hardness testing, and corrosion testing. Macroscopic observations of the samples revealed a range of stir zone shapes and defects that resulted from both inadequate and excessive heat input during the welding process. Analysis of the microstructure and results from the tensile testing indicated that the specimens produced using FSW settings of 2000 rpm and 40 mm/min achieved a peak ultimate tensile strength, demonstrating a value of 150 MPa. The micro-hardness values exhibited variations corresponding to changes in rotational speed, attaining a peak value of 240 HV at a rotational speed of 2300 rpm and a travel speed of 40 mm/min. The best mixing of the joined materials was achieved at a maximum welding rotational speed (2300 rpm) and medium travel speed (40 mm/min). A corrosion analysis of welded joints was conducted using a potentiodynamic polarization test in a solution containing 3.5% sodium chloride (NaCl). The welded zone (WZ) exhibits a reduced corrosion current density (I_{corr}), attributed to the occurrence of galvanic corrosion. The performance of corrosion within the WZ is impacted by the rotational speed and tool travel speed. Lowering the speed of the rotation tool leads to a decrease in the corrosion rate. Optimal corrosion resistance is achieved in the joint created at 2300 rpm and 30 mm/min, attributable to the suitable density and size of precipitates.

KEYWORDS: Joining dissimilar alloys, friction stir welding, microstructural analysis, mechanical characteristics.

Effect of Welding Settings on Mechanical Characteristics, Microstructural Features, and Corrosion Performance in Friction Stir Welding of Dissimilar AA6082-T6/7075-T6 Joints

<div dir="rtl">

تأثير إعدادات اللحام على الخصائص الميكانيكية والبنية المجهرية وأداء التآكل الكيميائي لوصلات اللحام الاحتكاكي لسبيكتي الألمونيوم AA6082-T6 و AA7075-T6

رشا محمد عفيفي، محمد جميل

قسم الهندسة الميكانيكية - كلية الهندسة بشبرا - جامعة بنها – القاهرة – مصر

*البريد الاليكتروني للباحث الرئيسي : rash.ali@feng.bu.edu.eg

الملخص

تستكشف هذه الدراسة تأثير إعدادات اللحام (سرعة دوران الأداة، التغذية) على الخصائص الميكانيكية (الشد، الصلادة المجهرية)، والبنية المجهرية، وأداء التآكل لوصلات اللحام المتباينة بين سبائك الألومنيوم AA7075-T6 وAA6082-T6، والتي تم تصنيعها بواسطة اللحام الاحتكاكي. تأخذ الدراسة في الاعتبار ثلاث سرعات دوران متغيرة للأداة (1600، 2000، و2300 دورة في الدقيقة) بالتوافق مع ثلاث قيم للتغذية (30، 40، و50 م/دقيقة). تم إنشاء وصلات اللحام عن طريق لحام صفائح بسماكة 6 م. خضعت العينات الملحومة للتوصيف من خلال المجهر الضوئي، المجهر الإلكتروني الماسح، اختبارات الشد، اختبارات الصلادة المجهرية، واختبارات التآكل. كشفت الملاحظات المجهرية للعينات عن مجموعة من أشكال منطقة الخلط والعيوب الناتجة عن كل من نقص وزيادة الحرارة المدخلة أثناء عملية اللحام. أشار تحليل البنية المجهرية ونتائج اختبار الشد إلى أن العينات المنتجة باستخدام إعدادات اللحام الاحتكاكي بسرعة 2000 دورة في الدقيقة و40 م/دقيقة حققت قوة شد نهائية ذروية، مظهرة قيمة 150 ميجا باسكال. أظهرت قيم الصلادة المجهرية تغيرات تتوافق مع التغيرات في سرعة الدوران، محققة قيمة ذروة 240 HV عند سرعة دوران 2300 دورة في الدقيقة وسرعة سفر 40 م/دقيقة. تم تحقيق أفضل خلط للمواد الموصولة عند أقصى سرعة دوران للحام (2300 دورة في الدقيقة) وتغذية متوسطة قدرها 40 م/دقيقة. وقد أجري تحليل التآكل لوصلات اللحام باستخدام اختبار الاستقطاب البوتنسيوديناميكي في محلول يحتوي على 3.5% من كلوريد الصوديوم. وأظهرت المنطقة الملحومة كثافة تيار تآكل منخفضة ناتجة عن حدوث عملية التآكل الكيميائي. يتأثر أداء التآكل داخل المنطقة الملحومة بسرعة دوران الأداة والتغذية. ويؤدي خفض سرعة أداة الدوران إلى انخفاض في معدل التآكل. كما تُحقق أفضل مقاومة للتآكل في الوصلة المُنشأة عند سرعة 2300 دورة في الدقيقة وتغذية 30 م/دقيقة، ويُعزى ذلك إلى الكثافة وحجم الرواسب المناسبة.

الكلمات المفتاحية : لحام سبائك مختلفة، لحام الاحتكاك والخلط، تحليل البنية المجهرية، الخصائص الميكانيكية.

</div>

1. INTRODUCTION

Aluminum alloys stand out in various applications, distinguishing themselves from alternative materials due to their malleability, allowing for the facile shaping of diverse structures through straightforward mechanical processes. The utilization of aluminum alloys is essential in crafting vehicle bodies, as well as in the production of heat exchanger units, aerospace components, thermal unit boiler constructions, and all boiler accessories [1,2].

Traditional welding techniques struggle with joining aluminum alloys due to strength loss [3 – 5]. However, advanced solid-state joining methods like FSW have demonstrated efficacy in producing high-quality welds, even in materials challenging for conventional fusion welding [6 – 8]. In FSW, the tool performs two main functions: producing heat and aiding the flow of material. The interaction between the tool rotational speed and the workpiece frictionally softens the material without causing it to melt, and the low temperature resulting from friction minimizes contractions during solidification and cooling, reducing distortions. This process is simpler compared to using fillers or gas shields [9, 10].

The selection of varied materials for different components as structural elements depends on the specific performance criteria influenced by operational conditions, the manufacturing process, and production expenses. Consequently, welding dissimilar

aluminum alloys becomes necessary, particularly for alloys like 6xxx and 7xxx, with the latter being highly prevalent in the transportation and automotive sectors, accounting for a substantial weight percentage [11, 12]. The 6xxx series offers good formability, moderate strength, and high corrosion resistance, The 7xxx aluminum alloys demonstrate superior strength performance compared to all other commercially available aluminum alloys. Through thermal treatment processing and an improved strength-to-weight ratio, these alloys emerge as potential alternatives to steel in the automotive sector [13].

The welding settings of FSW with a focus on joining aluminum alloys 6061-T6 and 7075-T6 with a thickness of 4.76 mm. The research focused on improving joint quality by incorporating programmed tool offsets and monitoring dynamic temperatures at the tool–workpiece interface during welding. The study clarified the influence of alloy positioning and weld tool offset on the joint. The findings indicated that strengthening the joint can be accomplished by decreasing the welding temperatures and increasing the incorporation of AA7075 into the nugget zone (NZ) [14].

Additionally, the impact of welding settings on FSW joints involving aluminum alloys AA6101-T6 and AA7075-T651. Their analysis of tensile behavior, hardness, and wear demonstrated a positive correlation between the increase in travel speed and the rise in ultimate tensile strength (UTS). Conversely, UTS decreased with higher rotational speed values. Fracture analysis revealed that all specimens experienced failure in the heat affected zone (HAZ) in proximity to the AA6101-T6 alloy. The micro-hardness exhibits variability within the HAZ and NZ under consistent rotational and travel speeds. The highest wear resistance occurred at a rotational speed of 1850 rpm and a welding speed of 65 mm/min. In contrast, improved material mixing occurred in the NZ of the welded specimens at 1250 rpm and 110 mm/min [15].

A computerized numerical control (CNC) machine to join AA6061 and AA7075 aluminum alloys through FSW [16]. Their study emphasized the use of optimal rotational speeds at 1250 rpm and a travel speed of 120 mm/min, leading to the production of welds without defects. In related research, Guo et al. [17] emphasized that increasing welding speed, leading to reduction in heat input, and enhanced material mixing conditions at the NZ when positioning the harder alloy (AA7075) on the retreating side and softer alloy (AA6061) on the advancing side the during FSW. Additionally, D.A. Dragatogiannis [18] reported that the thermal profile and material movement in FSW are affected by the arrangement of different materials on either the retreating or advancing side of the welds. These collective findings contribute to our understanding of optimizing FSW processes for dissimilar aluminum alloys.

Several researchers have explored the corrosion behavior of FSWed alloys [19–21]. In a study by Won V. Fahimpour et al. [22], the corrosion characteristics of AA6061 joined by FSW and gas tungsten arc welding (GTAW) were investigated. Their findings

revealed that corrosion resistance was superior in FSW grains compared to the GTAW structure. However, the WZ demonstrated increased vulnerability to corrosion when compared to the base metal (BM). This observation aligns with similar results reported by [23, 24]. In contrast, Peng Dong [25] presented results suggesting that the BM is especially prone to intergranular corrosion, primarily due to the uninterrupted formation of Si and Q phases, which are cathodic, along the boundaries of the grains coupled with the absence of precipitates along the grain boundaries in the precipitate-free zone. Another study by Ales et al. [26] focused on the impact of FSW on the corrosion behaviors of AA2024-T4 aluminum alloy. The study emphasized that corrosion initiation took place at locations associated with FSW, and the sizes of localized corrosion increased over time. These collective investigations contribute valuable insights into the corrosion dynamics of friction stir-welded alloys.

Science the welding of AA6082-T6 and AA7075-T6 by FSW also poses some challenges, such as the selection of optimal process parameters, the control of material flow and mixing, the characterization of microstructure and mechanical properties, and the understanding of the failure mechanisms [27 – 30]. So, this research endeavors to assess the impact of two primary factors, namely rotational tool speed and travel tool speed, on the microstructure, mechanical characteristics, and corrosion behavior of dissimilar FSWs. The investigation focuses on characterizing welds between materials with high mechanical strength (AA7075-T6) and elevated resistance to fresh and saltwater corrosion (AA6082-T6), representing commercial aluminum alloys. The primary objective is to explore the feasibility of joining dissimilar metals (AA7075-T6 and AA6082-T6) and augmenting welding strength through the optimization of process parameters. The selection of these parameters and their respective ranges is grounded not only in literature support but also in trial experiments.

Selecting AA6082-T6 and AA7075-T6 for joining by FSW is strategic due to their distinct properties. AA6082-T6 is known for its excellent corrosion resistance, strength, and machinability, making it ideal for structural applications. 7075-T6, on the other hand, offers superior strength but is more prone to corrosion. FSW allows for the effective joining of these alloys, leveraging the strengths of each while mitigating their weaknesses. This method provides robust, high-quality welds, essential for applications demanding high strength and durability, such as in the aerospace and automotive industries. The welding of these two alloys by FSW can achieve a balance between strength and ductility, and improve the performance and efficiency of the structures [28 – 31].

2. MATERIAL AND EXPERIMENTAL PROCEDURES

The materials used in current investigation are aluminum alloy AA6082-T6 and AA7075-T6, the two-rectangle plate of dimension 200×100×6 mm butt welded by friction

stir welding, The chemical composition of the aluminum alloys is presented in **Table 1**, while **Table 2** provides the mechanical characteristics. A taper cylindrical threaded tool is used in the FSW which is made of quenched and tempered tool steel (K110) after heat treatment, the tool chemical composition in presented in **Table. 3**, FSW tool has 4.5 mm pin length and a concave shoulder with diameter 16 mm as illustrated in Figure. 1. The two plates are joined together by a butt weld where the FSW process perpendicular to the plates' direction. Dissimilar FSW process was occurred by positioning the low strength aluminum alloy (AA6082-T6) at the advancing side (AS) and the high strength aluminum alloy (AA7075-T6) at the retreating side (RS), Positioning the weaker alloy at the RS results in a stronger weld region compared to when the low-strength alloy is placed at the AS [8].

A CNC milling machine, denoted as LMV 800, equipped with a primary power motor rated at 11 kW and operating at 380 V, possessing a maximum rotational speed of 10000 rpm. This milling machine is employed for FSW applications through the utilization of a fixture.

Table .1 The weight percentage of elements in the alloy compositions of AA 6082-T6 and AA 7075-T6.

Base alloys	Mg	Si	Fe	Ti	Zn	Cr	Cu	Mn	Al
AA6082-T6	0. 735	1.5	0.299	0.0229	0.0360	0.0027	0.0639	0.743	96.5
AA7075-T6	2.37	0.106	0.273	0.0296	5.65	0.197	2.62	0.0412	88.6

Table. 2 Mechanical characteristics of AA6082-T6 and AA7075-T6 alloy.

Alloys	σ_y (MPa)	σ_u (MPa)	Elongation (%)	Microhardness
AA6082-T6	241	205	12	108
AA7075-T6	526	528	12	171

Table. 3 Chemical composition of tool steel K110 (wt. %).

| Elements	C	Fe	Mn	P	S	Cr	Mo	V
W%	1.81	85.42	0.226	0.0243	0.0084	11.01	0.75	0.75
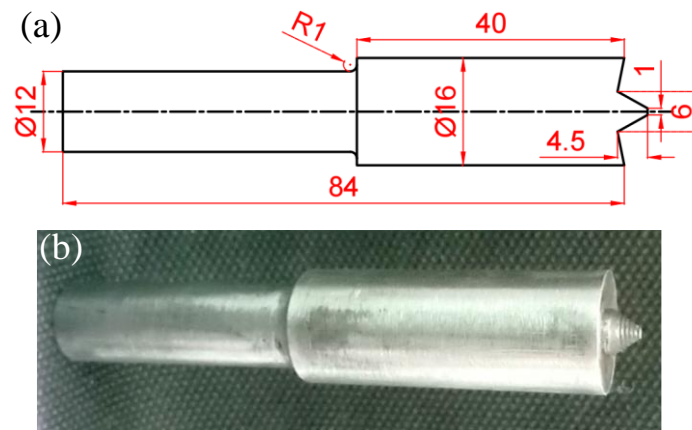
Fig. 1. Tool (a) Engineering drawing (b) Real image.

In **Fig. 2 (a),** the fixture is securely affixed to the milling machine table to mitigate vibrations arising from the frictional forces inherent in the welding process. Fig. 2 (b) shows the two aluminum alloys AA6080-T6 at the AS and AA7075-T6 at the RS after the FSW process. In addition, **Fig. 3** presents a schematic illustration for the FSW process for the two welded Aluminum alloys showing the AS and RS and the position of the cut tensile test sample within the welding zone. Experimental trials are conducted to ascertain the operational characteristics and permissible ranges of these process parameters. The outcomes of these trials are summarized in **Table 4**, presenting the influenced process parameters and their respective working ranges for dissimilar FSW involving AA6082-T6 and AA7075-T6 materials.
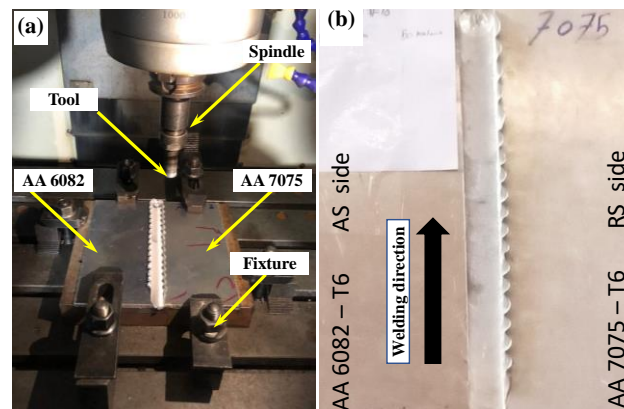
Fig. 2. (a) FSW set up and (b) Welding specimen.
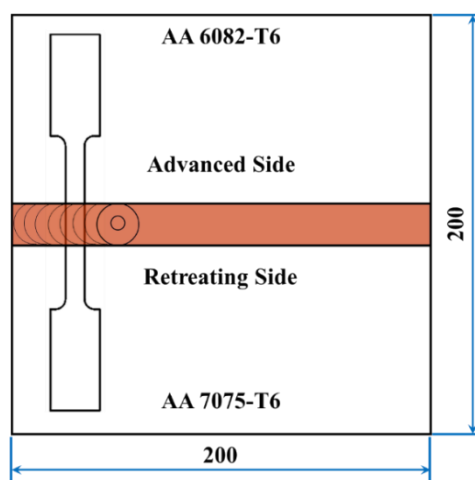
Fig. 3. Tensile test specimen across the welding joint between AA 6082-T6 and AA 7075-T6

Table. 4 Friction stir welding parameters.

Travel Speed (mm/min)	Rotation Speed (rpm)		
	1600	2000	2300
30	S1	S2	S3
40	M1	M2	M3
50	H1	H2	H3

All joints underwent perpendicular cross-sectional cutting in relation to the welding direction to facilitate subsequent metallographic analysis. The metallographic specimens' cross-sections were meticulously prepared using established metallographic techniques. This involved sequential grinding with silicon carbide sandpapers of varying grit sizes (400, 800, 1200, 2000, and 2300), followed by mechanical polishing utilizing a 0.3μm alumina suspension. Subsequently, the specimens were subjected to etching using Keller's reagent composed of 2 ml HF (48%), 3 ml HCL, 20 ml HNO_3, and 175 ml water. The resulting microstructures were then examined using an optical metallographic overturned microscope (OLYMPUS PMG 3).Transverse tensile strength assessments were conducted to appraise the mechanical characteristics of the welding joint. Tensile specimens were accurately sectioned along the longitudinal direction of the weld line, with the specimen's geometry and dimensions detailed in **Fig. 4** according to ASTM E8/E8M. The tensile tests were executed at room temperature utilizing a Universal Testing Machine. The UTS was determined by averaging the results from three specimens. Additionally, the yield strength was calculated from the stress strain curves generated by the machine, considering 0.2% strain. Micro-hardness testing was conducted using a Vickers micro-hardness machine with a 200-gram applied load for 10 seconds at 1mm intervals. The hardness measurements were obtained through a Micro-hardness tester.
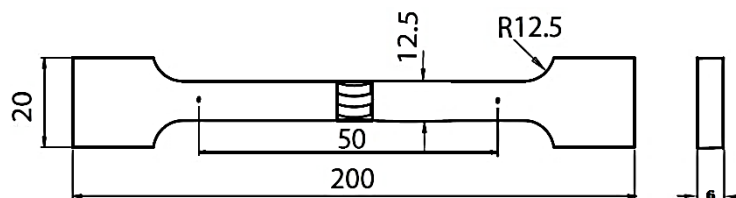
Fig. 4. Fabricated test specimen dimensions according to ASTM.

Corrosion tests were conducted in a 3.5 wt.% NaCl solution for a duration of 24 hours. The potentiodynamic polarization test occurred at room temperature, employing an electrochemical cell comprising three distinct electrodes. The experimental setup involved a working electrode, a platinum sheet is used as the counter electrode, while a saturated calomel electrode (SCE) serves as the reference electrode. Specimens, prepared by cutting and grinding to a 2000 grit finish, had their sides and backs insulated with Teflon to ensure that only the exposed surfaces interacted with the solution. Evaluation of I_{corr} and corrosion potential (E_{corr}) involved fitting the data from the polarization curves using a Tafel-type approach.

1. Results and Discussions

3.1 Macro and Microstructural Examination

Table 5 displays the surface features and macroscopic structures of AA7075/6082 FSW joints, which were produced using the taper-threaded pin and varying welding parameters. Examination of the upper surface of the welds revealed predominant semicircular features and distinct ribbon flashes in most joints. Macroscopic analysis of the nine FSW joints highlighted variations in macrostructures influenced by welding parameters, and certain welds exhibited discernible inner defects. The macrographs of all specimens exhibit uneven material distribution from the higher section of the WZ to the lower section, as indicated in **Table 5**. This nonuniformity may stem from fluctuations in the contacting surface between the tool pin and the welded materials, attributed to the taper threaded tool pin configuration employed during welding. The application of Weck's reagent highlights a lighter color for 7075-T651 and a darker color for 6082-T6.

Sample S1 displays the minimal level of blending; furthermore, macrostructure examinations indicate the presence of a cavity defect predominantly located at the bottom of the joints. Reduced heat input results in increased flow stresses, Resulting in insufficient material displacement and impeding material consolidation. In contrast, joints S2 and S3 facilitate a clearer identification of the distinctive shape of the FSW joints.

The FSW AA7075/AA6082 joints M1, M2, M3 exhibited a well-blended area without surface cavity defects. Conversely, the examination of FSW joint photos was

carried out with an optimal level of mixing. Elevating the feed rate to 50 mm/min led to flawed FSW AA7075/AA6082 joints for specimens (H1, H2, H3), leading to hole defects. These defects formed at this feed speed level resulted from inadequate heat input. It can be deduced that employing the highest welding speed in the study led to the occurrence of wormhole defects, primarily attributable to insufficient material flow and a deficiency in joint filling.

Fig. 5 illustrates a macrostructure example of the FSW joint for sample S1 of AA7075/AA6082, depicting characteristic zones. This welding joint was created with a rotational speed of 1600 rpm and a transverse speed of 30 mm/min. Macro observations revealed asymmetry on both sides of the weld, attributed to the inherent characteristics of the process. Microscopic examination further indicated a lack of substantial material mixing.

A minimal amount of material from one side is transferred to the other side of the NZ [35]. Different zones are noticeable in the weld, attributed to the temperature gradient across the weld cross-section and significant uniform deformation [36].

Microscopic observations revealed distinct zones: the HAZ, the thermomechanical affected zone (TMAZ), the pin affected nugget zone (PANZ), and the shoulder affected nugget zone (SANZ) on either flank of the joint. Figure 5 illustrates these regions, with the SANZ zone located in the upper third of the welding zone and the PANZ zone occupying approximately two-thirds of the lower nugget joint. These regions are designated as follows: A - base material in the AA7075 edge, B - TMAZ/HAZ in the AA7075 edge, C - SANZ in the AA7075 edge, D - SANZ/PANZ border in the AA7075 edge, E - SANZ in the center, F - PANZ in the AA7075 edge, G - PANZ in the AA6082 side, H—SANZ/PANZ border from the AA6082 perspective, I—SANZ from the AA6082 edge, J and K - TMAZ/HAS in the AA6082 edge.

Table 5. Surface characteristics and macrostructures of FSWed joints in AA7075-T6 and AA 6082-T6.

Sample No.	Surface Morphology	FSW joints Macrostructure
S1		
S2		
S3		
M1		
M2		
M3		
H1		
H2		
H3		
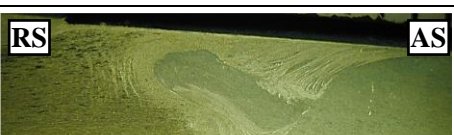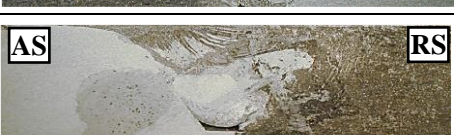
Delineating the boundary between the TMAZ and HAZ through optical microstructural observation proves challenging, making it difficult to precisely identify the termination of the HAZ toward the BM. Nevertheless, the demarcation between the TMAZ and the Pin-Affected Nugget Zone/Shoulder-Affected Nugget Zone (PANZ/SANZ) is readily noticeable thanks to the uniform size and morphology of the grain (Fig. 5 C, D, J). The observation suggests that multiple layers of materials from the

AS (6082-T6) of the weld seem to be more extensively integrated into the 7075-T6 on the RS at the weld regions (Fig. 5, F, G, H).

Fig. 6 illustrates the grain refinement compared to the base materials. Panel (A) provides a clear view of the shoulder-affected zone and pin-affected zone from the AA7075 side. Panel (B) showcases the microstructure of the TMAZ and HAZ from the AA7075-T6 side, while Panel (C) displays the microstructure of the TMAZ and HAZ from the AA6082-T6 side.
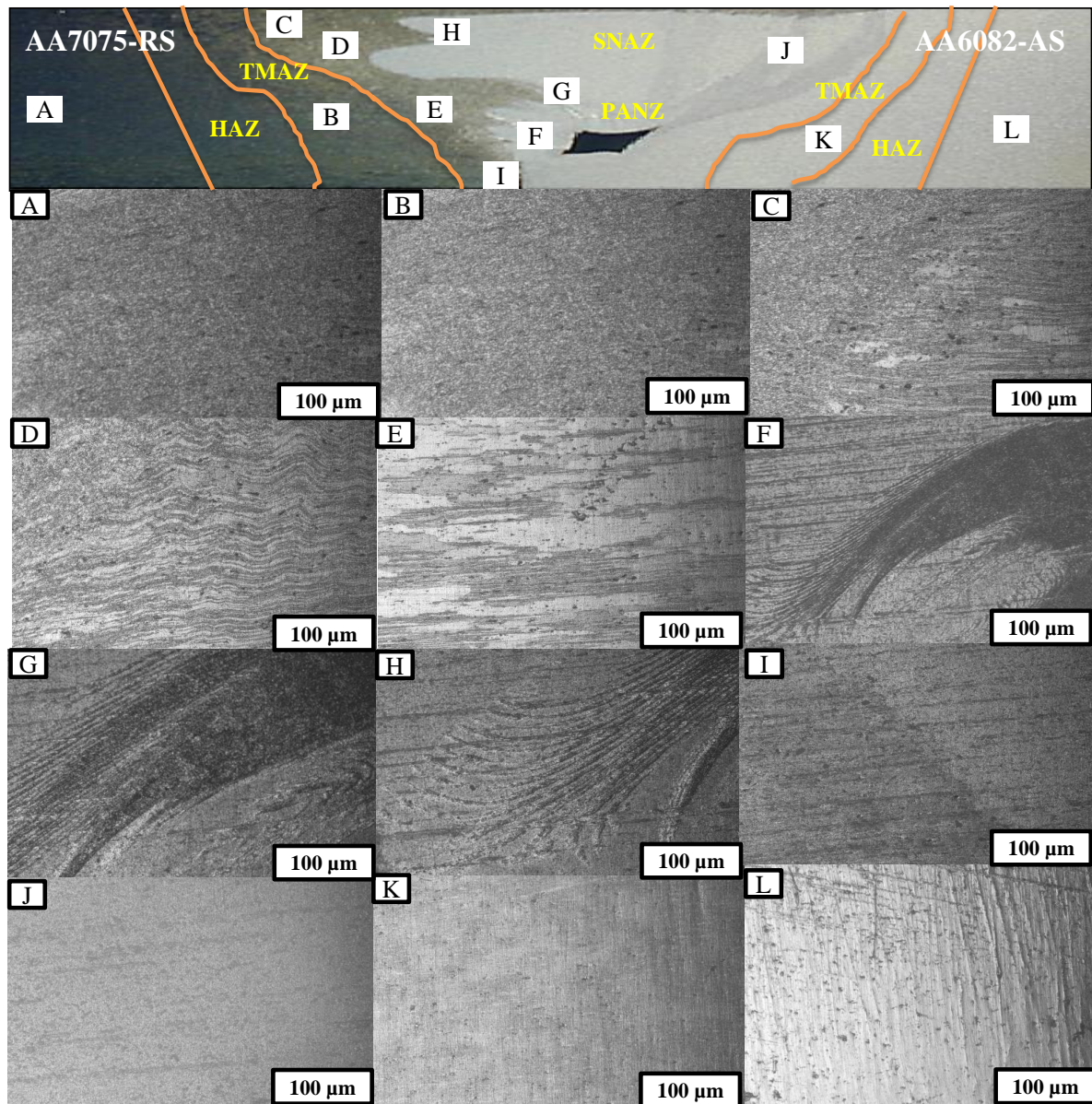

Fig. 5. Microstructure of Different welded region at 1600 rpm and 30 mm/min.
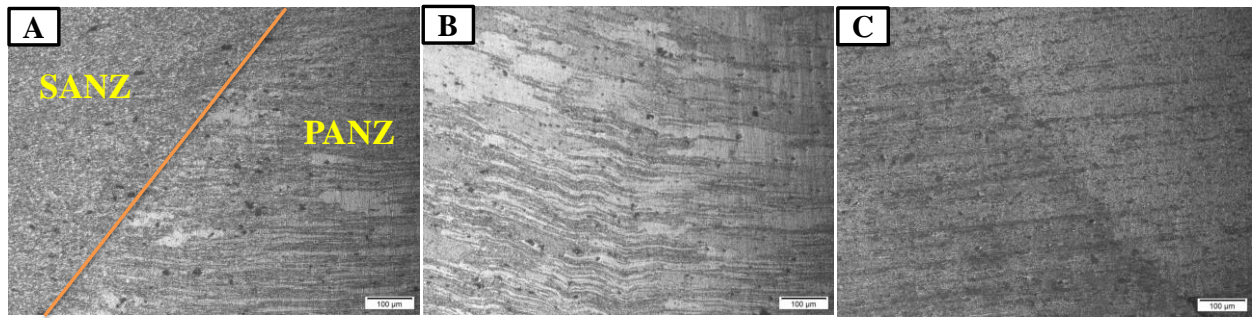
Fig. 6. Microstructure of (a) SANZ + PANZ, (B) The microstructure of TMAZ and HAZ from the side AA 7075-T6 shown in (B), (C) TMAZ and HAZ from the side AA 6082-T6 in S1 sample.

3.2 Mechanical Behavior

3.2.1 Tensile Testing

Table 6 tabulates the measured tensile strength values for the purposed welding conditions presented in **Table 4.** In addition, **Fig. 7** shows the tensile strength values in a bar chart to provide a clear comparison between the measured tensile strength values with respect to the applied travel speeds (30 mm/min, 40 mm/min, and 50 mm/min), and rotational speeds (1600 rpm, 200 rpm and 2300 rpm). It was noticed that the maximum measured tensile strength was attained at a travel speed of 40 mm/sec and a rotational speed of 2000 rpm.

Table 6. Tensile strengths of FSW plates AA 7075-T6 and AA 6082-T6.

| Experiment No	1	2	3	4	5	6	7	8	9
Travel speed (mm/min)	30			40			50		
Rotational speed (rpm)	1600	2000	2300	1600	2000	2300	1600	2000	2300
Tensile strength (MPa)	95	68	81	57	150	100	88	87	77
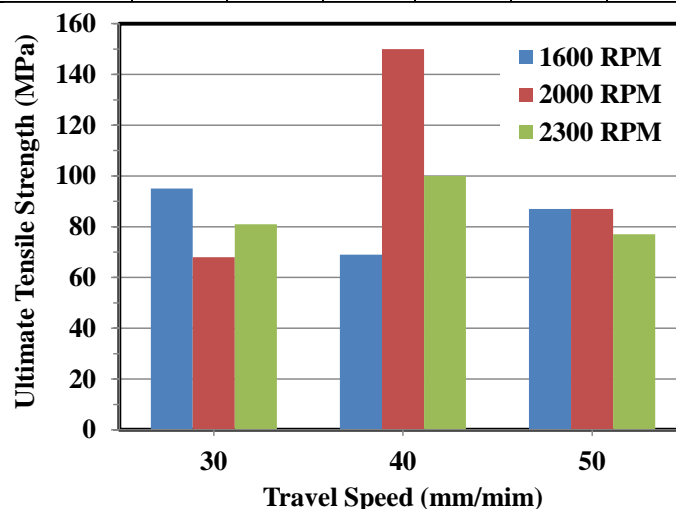
Fig. 7. Influence of tool travel speed (mm/min) and rotational speed (rpm) on the UTS of the welded joints.

Aluminum Magnesium Silicon (Al-Mg-Si) Phase: AA6082-T6 contains this phase, which contributes to its excellent strength and weldability. The presence of magnesium and silicon enhances the alloy's mechanical properties, making it suitable for structural applications where strength and formability are important [34].

Aluminum Zinc Magnesium Copper (Al-Zn-Mg-Cu) Phase: 7075-T6 is known for its high strength-to-weight ratio, primarily due to the presence of this phase. The addition of zinc, magnesium, and copper results in the formation of strengthening precipitates, such as the η (eta) and θ (theta) phases, which contribute to the alloy's exceptional strength [35].

The different phases in AA6082-T6 and 7075-T6 play a crucial role in determining their mechanical properties. In AA6082-T6, the Al-Mg-Si phase enhances strength and formability, making it suitable for structural applications requiring moderate strength and good weldability. Conversely, 7075-T6, with its Al-Zn-Mg-Cu phase, exhibits exceptionally high strength, making it preferred for applications demanding superior mechanical properties [36].

Figure 8 illustrates the failure locations of all the welded joints. The observation indicates that fracture takes place in the AS-HAZ, attributed to the accumulation of heat.
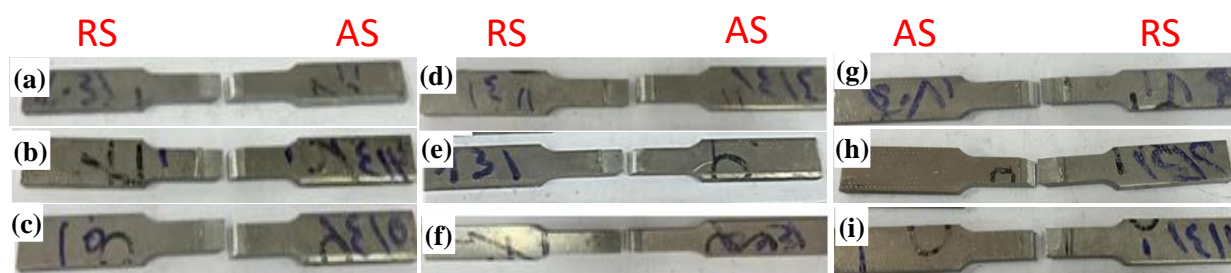
Fig. 8. Fracture specimen (a)1600 rpm, 30 mm/min (b) 2000 rpm, 30 mm/min (c) 2300 rpm, 30 mm/min (d) 1600 rpm, 40 mm/min (e) 2000 rpm, 40 mm/min (f) 2300 40 mm/min (g) 1600 rpm, 50 mm/min (h) 2000 rpm, 50 mm/min (i) 2300 rpm, 50 mm/min.

Fig. 9 displays a fracture surface characterized by dimples and voids of varying depths and sizes. This behavior is associated with ductile characteristics and the development of necking before fracture. The dimples surround the transgranular fracture surface. This may explain the restricted elongation during the tensile test and the absence of necking in the sample, as observed in joint AA6082-AA7075. Fig. 9 illustrates large void sizes formed after some deformation of dimples into a V-shape, possibly contributing to reduced strength and the degradation of superplastic deformation in materials. On contrary, the narrow and small dimple in **Fig. 10**.
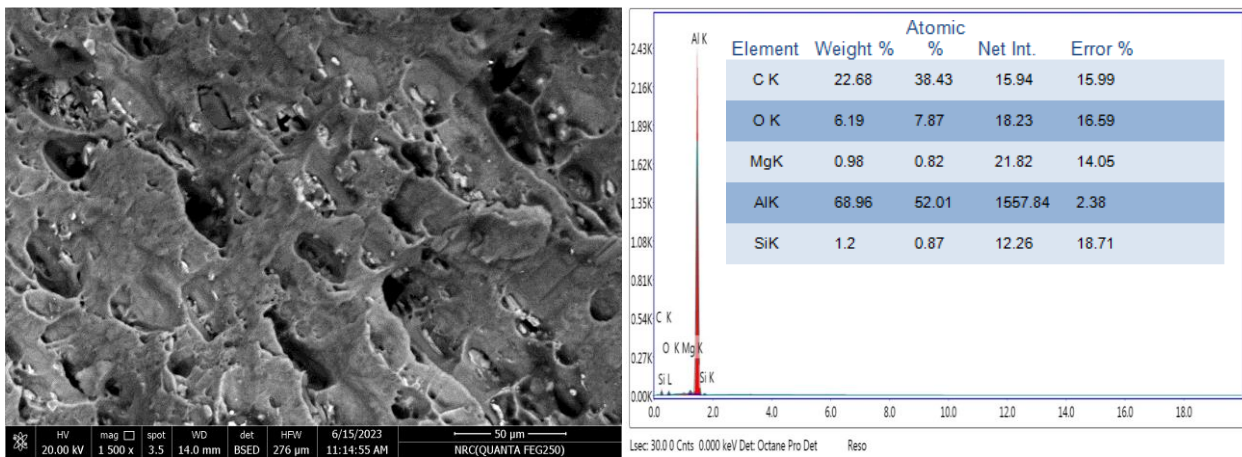
Fig. 9. SEM image and EDX within the fracture surface at 1600 rpm and 40 mm/min.
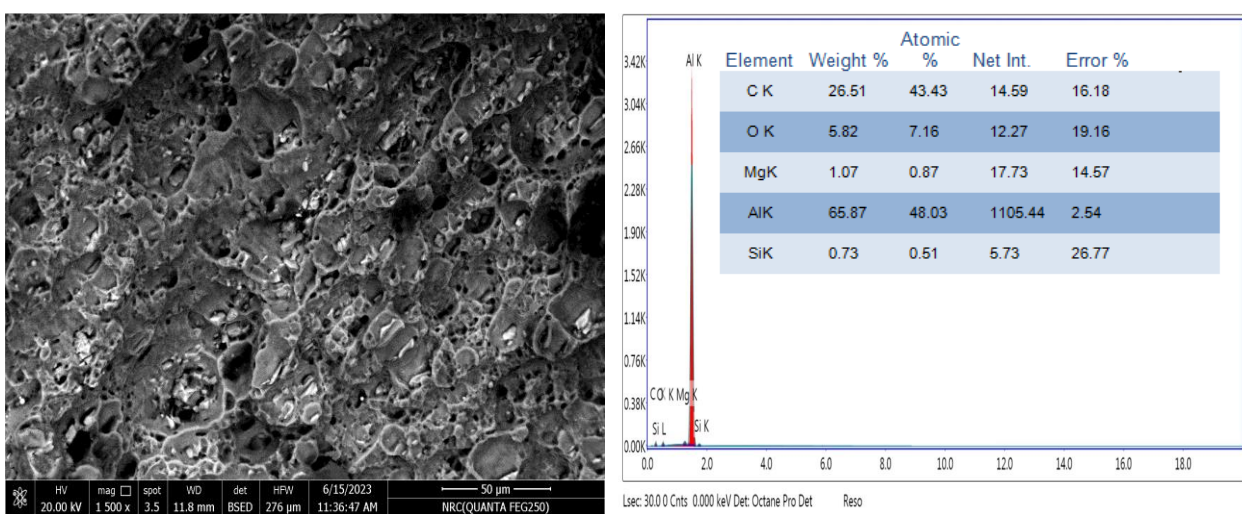
**Fig. 10.** SEM image and EDX within the fracture surface at 2000 rpm and 40 mm/min.

3.2.2. Hardness Test

The hardness profiles depicted in **Figs. 10, 11,** and **12** illustrate the variation across the middle thickness of welded joints, considering three rotational speeds and three travel speeds. The hardness distribution in all the joints reveals asymmetric distribution pattern, which is like that found in AA2024/7075 FSW joints [37]. Observations indicated a reduction in the micro-hardness of the BM within all HAZ for AS (6082-T6) alloys. Nevertheless, a slight elevation in the micro-hardness of the AA7075 alloy was observed towards the weld center, regardless of its location in the RS or AS. The highest measured micro-hardness value for the AA7075 alloy in NZ was 230 HV at 1600 rpm and 40 mm/min. This can be ascribed to solid solution strengthening resulting from the stirring of dissimilar alloys. [38]. Furthermore, the non-uniform microstructure within the NZ is formed because of the asymmetry of FSW, leading to variations in hardness values. These variations stem from differences in microstructure characteristics controlled by welding parameters. despite the increase in the micro-hardness of

aluminum alloys was rare. Mishra et al. [39] reported results indicating a slight rise in micro-hardness within the weld nugget compared to the TMAZ for marginally (less than 6%) hardened 5083-H112. This phenomenon is attributed to the formation of an extremely fine grain size FSW.
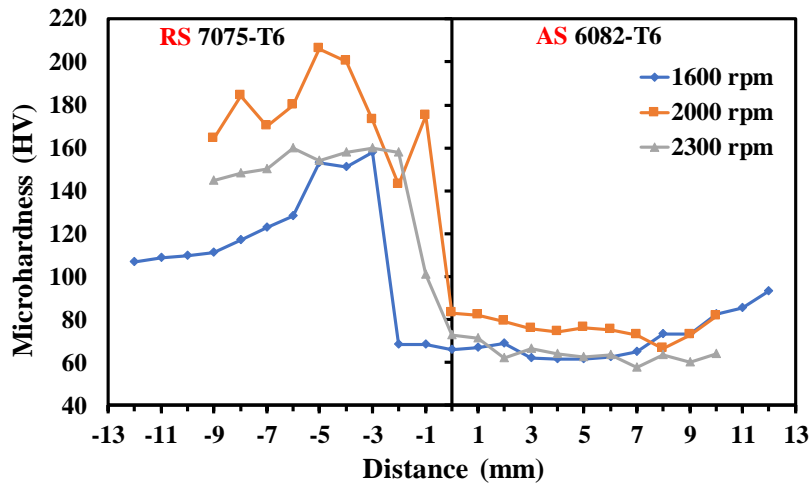

Fig. 10. Micro-hardness characteristics in the direction of central axis of the joint thickness at 30 mm/min.
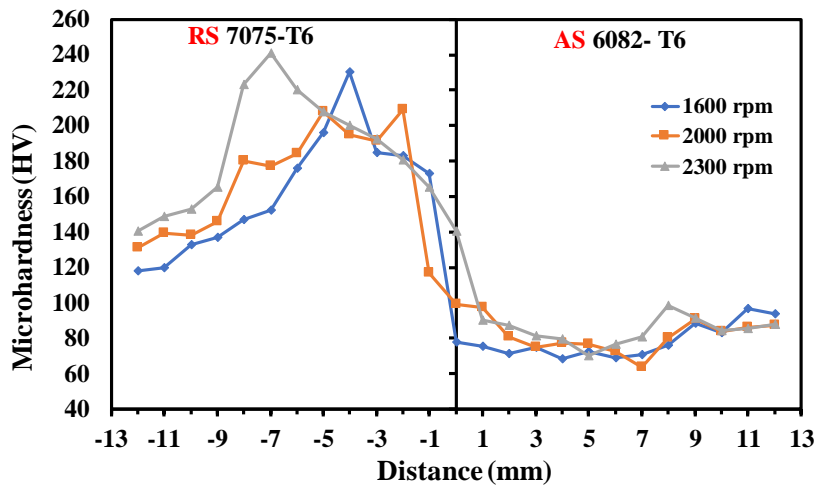

Fig. 11. Micro-hardness characteristics in the direction of central axis of the joint thickness at 40 mm/min.
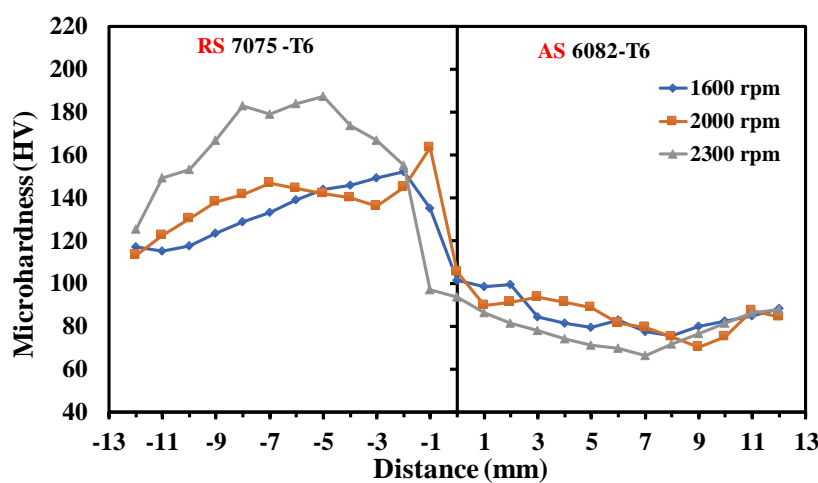

Fig. 12. Micro-hardness characteristics in the direction of central axis of the joint thickness at 50 mm/min.

3.2.3. Corrosion Behavior

The results of the Tafel curves are illustrated in **Fig. 13.** In addition, the corresponding measured values are outlined in **Table 6**. The I_{corr} and E_{corr} provide insights into the kinetic and thermodynamic tendencies of the specimen, collectively reflecting the corrosion behavior. Thus, the I_{corr}, E_{corr}, and Tafel slopes are also documented.

Fig. 13 (A) display the E_{corr} of the base material (BM) and NZ at different rotational speed (1600 rpm, 2000 rpm, and 2300 rpm) and constant speed 30 mm/min traverse speed, it is cleared from the figure that, At varying rotational speeds, the E_{corr} of a FSWed joint displays distinct values: 1426.5 mV at 1600 RPM, 814 mV at 2000 RPM, and 1013 mV at 2300 RPM. These measurements are all lower than the BM 6082's E_{corr} of 1484.2 mV, indicating a favorable outcome for the FSWed joint's corrosion resistance.

Fig. 13 (B) presents the E_{corr} for the BM and the NZ at a travel speed of 40 mm/min across different rotational speeds. The E_{corr} was recorded as 720 mV at 1600 rpm, 1403 mV at 200 rpm, and 1455.9 mV at 2300 RPM. The highest corrosion resistance was observed at 1600 rpm with a value of 18.7 kΩ/cm², while the lowest was at 2300 rpm, measuring 0.25 kΩ/cm². These findings are consistent with those reported in reference [40].

Fig. 13 (C) shows the E_{corr} of the base material (BM) and nugget zone (NZ) at a travel speed of 50 mm/min for different rotational speeds: 1365.3 mV at 2600 RPM, 1432.6 mV at 2000 RPM, and 1415.7 mV at 2300 RPM. These results indicate that the corrosion rate tends to increase as the rotational speed of the tool increases.

The corrosion resistance of a FSWed joint in aluminum alloys 6082-T6/7075-T6 improves significantly compared to the BM. A more negative Ecorr and a higher Icorr density indicate a greater tendency for corrosion [43]. In this case, a notably higher negative Ecorr value of 1455.9 mV and a higher Icorr density of 174.3 µAcm⁻² were observed at 40 mm/min and 2300 rpm, indicating lower corrosion resistance. Conversely, a less negative Ecorr value of -720.4 mV at 40 mm/min and 1600 rpm showed higher corrosion resistance of 18.07 kΩ/cm², which is significantly higher than the BM's 0.595 kΩ/cm². This demonstrates that dissimilar FSW can enhance the corrosion behavior of these aluminum alloys.
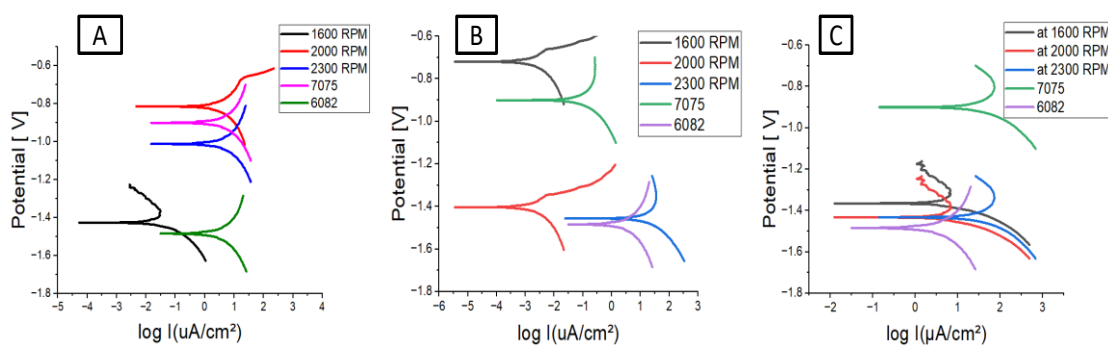

Fig. 13. Tafel curve of BM and SZ at different speed a) at 30 mm/min, b) 40 mm/min. and c) at 50 mm/min.

The presence of magnesium and silicon also improves the corrosion resistance of AA6082-T6 (See Fig. 9 and Fig. 10). However, it's important to note that the corrosion resistance of this alloy can still be affected by environmental factors, such as exposure to aggressive chemicals or saltwater environments. While 7075-T6 is more susceptible to corrosion compared to AA6082-T6. The presence of copper can make the alloy more prone to localized corrosion, especially in environments containing chloride ions [42].

The corrosion properties of AA6082-T6 and 7075-T6 are influenced by the alloy's composition and the types of phases present. While both alloys offer good corrosion resistance, AA6082-T6 generally has better resistance due to its lower copper content and the presence of magnesium and silicon, which provide protective oxide layers. However, 7075-T6, with its higher copper content, can be more susceptible to localized corrosion, especially in aggressive environments [43, 44].

Table 6. Electrochemical parameters measurements for the base alloys AA7075-T6 and AA6061-T6, along with the FSW zones produced under various welding conditions.

Travel speed (mm/min)	Rotational speed (rpm)	-E(mV) vs SCE	I_{Corr} (μAcm^{-2})	Polarization resistance ($k\Omega/cm^2$)	Corrosion rate ($\mu m/y$)
AA 7075- T6		900.2	6.5	8.91	70.302
AA 6082- T6		1484.2	77.6	0. 595	845.55
30	1600	1426.5	200.6	0.75733	2184.7
	2000	814.4	4.75	7.71	51.713
	2300	1013	4.71	11.96	51.301
40	1600	720.4	5.1	18.07	55.651
	2000	1403	28.7	1.41	312.56
	2300	1455.9	174.3	0.25150	1898.0
50	1600	1365.3	50.2	2.76	546.72
	2000	1432.6	47	0.70326	511.96
	2300	1415.7	98.5823	0.73704	1073.6

SUMMARY AND CONCLUSIONS

In this ongoing study, two distinct sheets of aluminum alloys, specifically AA6082-T6 and AA7075-T6, each possessing a thickness of 5 mm, underwent FSW utilizing varying rotational speeds (1600, 2000, and 2300 rpm) and travel speeds (30, 40, and 50 mm/min). The welding process was facilitated by the utilization of a specialized tapered thread tool. After the welding procedure, a comprehensive assessment of the efficacy of the welded joints was conducted through a series of tests, encompassing tensile tests, micro-hardness tests, and corrosion resistance analyses. Furthermore, detailed analyses of the microstructure in distinct regions, including the HAZ, TMAZ, SANZ, and BM were meticulously undertaken. Key findings include:

1. The peak tensile strength, reaching 150 MPa, was attained at a rotational speed of 2000 rpm and a travel speed of 40 mm/min. In contrast, the lowest measured UTS

of 68 MPa was noted at a tool rotational speed of 2000 rpm and a travel speed of 30 mm/min.

2. The highest measured microhardness value, reaching 230 HV, was recorded at 1600 rpm tool rotational speed and 40 mm/min travel speed. Conversely, the lowest micro-hardness (158 HV) was measured at a rotational speed of 2300 rpm and a travel speed of 30 mm/min.

3. The corrosion resistance of 6082-T6 was found to be notably higher than that of AA 7075-T6. The optimum conditions for achieving high corrosion resistance were identified at a tool rotational speed of 1600 rpm and a travel speed of 40 mm/min, with a corresponding voltage value of -1.46V.

ACKNOWLEDGMENTS

CONFLICT OF INTEREST

The authors have no financial interest to declare in relation to the content of this article.

REFERENCES

1. Kadaganchi R, Gankidi MR, Gokhale H (2015) Optimization of process parameters of aluminum alloy AA 2014-T6 friction stir welds by response surface methodology. Defence Technology 11:209–219.

2. Jijin Xu , Shuai Wang , Ze Chai , Jie Hong , Xiaohong Sun , Jiaxin Du , Yuxin Miao , Hao Lu (2022) Characterization and modeling of the hardening and softening behaviors for 7XXX aluminum alloy subjected to welding thermal cycle. Mechanics of Materials 172:104405.

3.Tomotake Hirata, Taizo Oguri, Hideki Hagino, Tsutomu Tanaka, SungWook Chung, Yorinobu Takigawa, Kenji Higashi (2007) Influence of friction stir welding parameters on grain size and formability in 5083 aluminum alloy. Materials Science and Engineering: A 456:344–349.

4. Rudrapati R (2019) Recent advances in joining of aluminum alloys by using friction stir welding. Mass Production Processes.

5. Shinde G, Dabeer P (2017) Review of experimental investigations in friction welding technique. Sustainable Development 373:384.

6. Mishra RS, Ma ZY (2005) Friction stir welding and processing. Materials science and engineering: R: reports 50:1–78.

7. Raturi M, Garg A, Bhattacharya A (2019) Joint strength and failure studies of dissimilar AA6061-AA7075 friction stir welds: Effects of tool pin, process parameters and preheating. Eng Fail Anal 96:570–588.

8. Sathari NAA, Razali AR, Ishak M, Shah LH (2015) Mechanical strength of dissimilar AA7075 and AA6061 aluminum alloys using friction stir welding. International Journal of Automotive and Mechanical Engineering 11:2713.

9. Raturi M, Garg A, Bhattacharya A (2019) Tensile strength and failure of dissimilar friction stir welded joints between 6061-T6 and 2014-T6 aluminum alloys. Procedia Structural Integrity 17:495–502.

10. Kar A, Singh K, Kumar L (2023) Effect of Tool Rotational Speed and Mechanisms Associated with Microstructure Evolution and Intermetallics Formation in Friction Stir Welding of Aluminum Alloy to Titanium Alloy. J Mater Eng Perform 1–12.

11. Varunraj S, Ruban M (2022) Investigation of the microstructure and mechanical properties of AA6063 and AA7075 dissimilar aluminium alloys by friction stir welding process. Mater Today Proc 68:1654–1657.

12. M. Tabasi, M. Farahani, M. K. Besharati Givi, M. Farzami, A. Moharami, (2016) Dissimilar friction stir welding of 7075 aluminum alloy to AZ31 magnesium alloy using SiC nanoparticles. The International Journal of Advanced Manufacturing Technology 86:705–715.

13. Dragatogiannis DA, Kollaros D, Karakizis P, et al (2019) Friction stir welding between 6082 and 7075 aluminum alloys thermal treated for automotive applications. Mater Perform Charact 8:571–589.

14. E. G. Cole, A. Fehrenbacher, N. A. Duffie, M. R. Zinn, F. E. Pfefferkorn, N. J. Ferrier (2014) Weld temperature effects during friction stir welding of dissimilar aluminum alloys 6061-t6 and 7075-t6. The International Journal of Advanced Manufacturing Technology 71:643–652.

15. Abolusoro OP, Akinlabi ET (2020) Effects of processing parameters on mechanical, material flow and wear behaviour of friction stir welded 6101-T6 and 7075-T651 aluminium alloys. Manuf Rev (Les Ulis) 7:1.

16. Hariharan R, Nimal R (2014) Friction stir welding of dissimilar aluminium alloys (6061&7075) by using computerized numerical control machine. Middle-East J Sci Res 20:601–605.

17. J.F. Guo, H.C. Chen, C.N. Sun, G. Bi, Z. Sun, J. Wei (2014) Friction stir welding of dissimilar materials between AA6061 and AA7075 Al alloys effects of process parameters. Materials & Design (1980-2015) 56:185–192.

18. Dragatogiannis DA, Kollaros D, Karakizis P, et al (2019) Friction stir welding between 6082 and 7075 aluminum alloys thermal treated for automotive applications. Mater Perform Charact 8:571–589

19. D. Sidane , E. Bousquet , O. Devos , M. Puiggali , M. Touzet , V. Vivier , Angeline Poulon-Quintin (2015) Local electrochemical study of friction stir welded aluminum alloy assembly. Journal of Electroanalytical Chemistry 737:206–211.

20. I.A. Kartsonakis, D.A. Dragatogiannis, E.P. Koumoulos, A. Karantonis, C.A. Charitidis(2016) Corrosion behaviour of dissimilar friction stir welded aluminium alloys reinforced with nanoadditives. Mater Des 102:56–67.

21. Esmaily, M., Mortazavi, N. , Osikowicz, W. , Hindsefelt, H. ,Svensson, J. E. , Halvarsson, M.;,Thompson, G. E. , Johansson, L. G. (2016) Corrosion behaviour of friction stir-welded AA6005-T6 using a bobbin tool. Corros Sci 111:98–109.

22. Fahimpour V, Sadrnezhaad SK, Karimzadeh F (2012) Corrosion behavior of aluminum 6061 alloy joined by friction stir welding and gas tungsten arc welding methods. Mater Des 39:329–333.

23. Farhad Gharavi, Khamirul Amin Matori, Robiah Yunus, Norinsan Kamil Othm, Firouz Fadaeifard (2015) Corrosion behavior of Al6061 alloy weldment produced by friction stir welding process. Journal of Materials Research and Technology 4:314–322.

24. Wadeson DA, Zhou X, Thompson GE, et al (2006) Corrosion behaviour of friction stir welded AA7108 T79 aluminium alloy. Corros Sci 48:887–897.

25. Dong P, Sun D, Wang B, et al (2014) Microstructure, microhardness and corrosion susceptibility of friction stir welded AlMgSiCu alloy. Materials & Design (1980-2015) 54:760–765.

26. Ales SK, Wang L (2017) Effects of friction stir welding on corrosion behaviors of AA2024-T4 aluminum alloy. In: MATEC Web of Conferences. EDP Sciences, p 02003.

27. Farzad Baratzadeh , Enkhsaikhan Boldsaikhan , Rajeev Nair , Dwight Burford , Hamid Lankarani (2020) Investigation of mechanical properties of AA6082-T6/AA6063-T6 friction stir lap welds. Journal of Advanced Joining Processes 1:100011.

28. Rudrapati R (2019) Recent advances in joining of aluminum alloys by using friction stir welding. Mass Production Processes.

29. M.Vetrivel Sezhian, K. Giridharan, D.Peter Pushpanathan, G. Chakravarthi, B. Stalin, Alagar Karthick, P. Manoj Kumar, Murugesan Bharani (2021) Microstructural and mechanical behaviors of friction stir welded dissimilar AA6082-AA7075 joints. Advances in Materials Science and Engineering 2021:1–13.

30. Fratini L, Buffa G, Filice L, Gagliardi F (2006) Friction stir welding of AA6082-T6 T-joints: process engineering and performance measurement. Proc Inst Mech Eng B J Eng Manuf 220:669–676.

31. Farzad Baratzadeh, Enkhsaikhan Boldsaikhan, Rajeev Nair, Dwight Burford, Hamid Lankarani(2020) Investigation of mechanical properties of AA6082-T6/AA6063-T6 friction stir lap welds. Journal of Advanced Joining Processes 1:100011.

32. Rémi Bertrand, Hugo Robe, Damien Texier, Yasser Zedan, Eric Feulvarch , Philippe Bocher(2019) Analysis of AA2XXX/AA7XXX friction stir welds. J Mater Process Technol 271:312–324.

33. Mahoney MW, Mishra RS (2007) Friction stir welding and processing. ASM International.

34. Raghavan V (2007) Al-Mg-Si (aluminum-magnesium-silicon). J Phase Equilibria Diffus 28:189–191.

35. HongfuYang,YelnZhang, ShanjuZhen, Zaki I.Zaki, Rensong Huang, Shumeng Lu, Peng Sun, Mohamed M. Ibrahim, Hua Hou3, Mengnie Li, Xiaohong Yuan, Xiaojing Wang,•Zeinhom M. El-Bahy (2023) Dissolution behavior of dizinc magnesium phase in Al–Zn–Mg–Cu alloy. Adv Compos Hybrid Mater 6:211.

36. Daniolos NM, Pantelis DI (2017) Microstructural and mechanical properties of dissimilar friction stir welds between AA6082-T6 and AA7075-T651. The International Journal of Advanced Manufacturing Technology 88:2497–2505.

37. Chenghang Zhang, Yuru Cao, G. Huang, Q. Zeng, Yulong Zhu, Xinde Huang, Nali Li, Qing Liu (2020) Influence of tool rotational speed on local microstructure, mechanical and corrosion behavior of dissimilar AA2024/7075 joints fabricated by friction stir welding. J Manuf Process 49:214–226.

38. Ilangovan M, Boopathy SR, Balasubramanian V (2015) Effect of tool pin profile on microstructure and tensile properties of friction stir welded dissimilar AA 6061–AA 5086 aluminium alloy joints. Defence Technology 11:174–184.

39. Mishra RS, Ma ZY (2005) Friction stir welding and processing. Materials science and engineering: R: reports 50:1–78.

40. Farhad Gharavi, Khamirul Amin Matori, Robiah Yunus, Norinsan Kamil Othman, Firouz Fadaeifard (2015) Corrosion behavior of Al6061 alloy weldment produced by friction stir welding process. Journal of Materials Research and Technology 4:314–322.

41. Mostafa Eldeeb, Lobna Khorshed, Sayed Abdallah, Ahmed Gaafer, Tamer Mahmoud (2019) Effect of friction stir welding process parameters and post-weld heat treatment on the corrosion behaviour of AA6061-O aluminum alloys. Egypt J Chem 62:1367–1375.

42. Patil HS, Soman SN (2014) Corrosion behaviour of friction stir welded aluminium alloys AA6082-T6. American Journal of Materials Engineering and Technology 2:29–33.

43. Rachele Bertolini, Enrico Simonetto, Luca Pezzato, Alberto Fabrizi, Andrea Ghiotti, Stefania Bruschi, (2021) Mechanical and corrosion resistance properties of AA7075-T6 sub-zero formed sheets. The International Journal of Advanced Manufacturing Technology 115:2801–2824.

44. Liu Y, Mol JMC, Janssen G (2016) Combined corrosion and wear of aluminium alloy 7075-T6. Journal of Bio-and Tribo-Corrosion 2:1–7.